In Situ Deposition of Hierarchical Architecture Assembly from Sn-Filled CNTs for Lithium-Ion Batteries

Xiaoyu Hou, Hao Jiang, Yanjie Hu,* Yunfeng Li, Junchao Huo, and Chunzhong Li*

Key Laboratory for Ultrafine Materials of Ministry of Education, School of Materials Science and Engineering, East China University of Science & Technology, Shanghai 200237, China

ⓈSupporting Information

ABSTRACT: In this paper, we have demonstrated a hierarchical architecture assembly from Sn-filled CNTs, which was in situ deposited on Cu foils to form binder-free electrode by incorporating flame aerosol deposition (FAD) with chemical vapor deposition (CVD) processes. The reversible capacity of Sn-filled CNTs hierarchical architecture anode exhibited above 1000 mA h g^{-1} before 30th cycle and stabilized at 437 mA h g^{-1} after 100 cycles at a current density of 100 mA g^{-1}. Even at as high as 2 A g^{-1}, the capacity still maintained 429 mA h g^{-1}. The desirable cycling life and rate capacities performance were attributed to great confinement of tin in the interior of CNTs and the superior conducting network constructed by the 3D hierarchical architecture. The novel, rapid and scalable synthetic route was designed to prepare binder-free electrode with high electrochemical performance and avoid long-time mixing of active materials, binder, and carbon black, which is expected to be one of promising preparation of Sn/C anodes in lithium-ion batteries.

KEYWORDS: flame synthesis, deposition, Sn-filled CNTs, hierarchical architecture, binder-free electrode, lithium-ion batteries
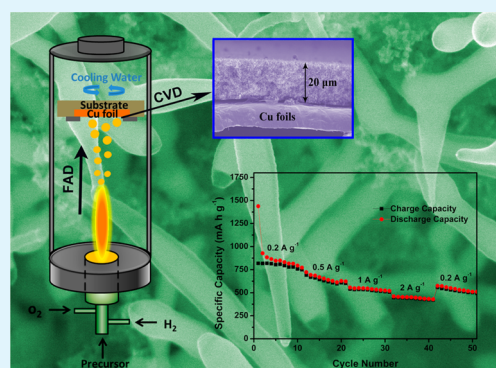
1. INTRODUCTION

Lithium-ion batteries (LIBs), because of their high energy density, long cycle life, rapid charging and discharging, high voltage, etc., have attracted much attention in industrial fields.[1-4] Nowadays, an increasing number of attempts have been made on developing a variety of electrode materials with hybrid compositions and novel structures to raise the energy density and cycling performance of rechargeable batteries.[5-7] In non-carbon-based anode materials, silicon (Si), germanium (Ge), and tin (Sn), which can incorporate relatively more Li$^+$ ions into alloy to achieve high theoretical capacity, have been increasingly focused. Compared to other materials, metallic tin with high theoretical specific capacity (992 mA h g^{-1}) and low price has been supposed to be one of promising anode materials in rechargeable lithium-ion batteries. However, a huge volume change (260%) in the metal alloying/dealloying processes of Sn reacting with Li could result in aggregation and pulverization, eventually leading to capacity fading tremendously and poor cycle performance. Several traditional strategies have been employed to overcome this drawback such as carbon coating, multiphase composites, particle size control, alloying etc.[8,9] Importantly, carbon coatings with the merits of excellent conductivity and tolerance to mechanical stress are supported to work as the buffering layer to suspend the volume expansion and improve electric conductivity of the matrix. Therefore, Sn/C nanocomposites have attracted more attention in employing as anode active materials in rechargeable LIBs. Sn/C hybrids with versatile morphologies, such as Sn@C nanocable, Sn@C nanorod, rambutan-like tin–carbon, tin nanoparticles dispersed in the carbon matrix, etc., have been successfully prepared.[10-14] Further, these anode materials show high reversible capacity and long-term cycle life. However, liquid-phase routes reported with low yields have limited their applications in the industry of LIBs. On the other hand, the assembly of electrode preparation needs binder, carbon black, and long-time mixing. Therefore, a novel approach for the synthesis of active materials and the assembly of electrode without binder and carbon black are still challenges in application of LIBs.

Flame aerosol techniques have been demonstrated to be an effective and industial route for preparation of nanomaterials.[15-17] Compared to the liquid-phase route, flame synthesis with advantages of being continuous, rapid, scalable, and without post-treatment can produce millions of tons of commodities like Al_2O_3, SiO_2, and TiO_2.[18,19] Nevertheless, flame-synthesis metal oxides are usually sphere particles and chainlike agglomerates rather than various nanostructures such as one-dimensional nanowires or core–shell structures. Because of rapid development and increasing attention on flame techniques, precise design for a variety of structures and functions of productions has been established and realized by multiple and particular synthetic devices.[20-23] Recently, flame

aerosol deposition (FAD) method has been developed for a variety of microsized membranes consisting of functional oxides. The obtained membranes show high porosity and versatile hierarchical architectures and exhibits promising potential in lithium-ion batteries, gas sensor, fuel cell, and so on.[24−27] Herein, novel hierarchical architectures in situ deposited on Cu foils assembly by Sn-filled carbon nanotube (CNT) have been fabricated by combining FAD technique and chemical vapor deposition (CVD) process. Briefly, hierarchical SnO_2 aerosols membranes on Cu foils was obtained by FAD approach. Then, the obtained SnO_2 membranes were reduced by C_2H_2 with CVD process. Eventually, hierarchical architectures of Sn-filled CNTs were fabricated. The as-prepared Sn-filled CNTs hierarchical architectures on Cu foils without binders and carbon black was employed as binder-free electrode and showed high reversible capacity of 437 mA h g^{-1} after 100 cycles at a current density of 100 mA g^{-1}. Even at as high as 2A g^{-1}, the capacity still maintained 429 mA h g^{-1}. The desirable cycling life and rate capacity performance were investigated and discussed in details.

2. EXPERIMENTAL SECTION

2.1. Synthesis of Sn-Filled CNT Hierarchical Architecture. In a typical experiment, water-free $SnCl_4$ was added into the bubble bottle employed as precursor. 160 mL min^{-1} H_2 and 80 mL min^{-1} O_2 was transported into flame nozzle to support flame combustion. Simultaneously, precursor was undergoing the center ring of flame nozzle by carrier gas of N_2 and reacting with O_2 to synthesize SnO_2 nanoparticles at the high flame temperature zone. In a certain 15 cm height of the nozzle, Cu foils located on the substrate with circulating cooling water was employed to in situ deposit the SnO_2 nanoparticles and the deposition process was maintained for 5 min. Afterward, the deposition SnO_2 membrane/Cu foils was transferred into tube furnace and heated to 600 °C at heating rate of 10 °C min^{-1} in Ar (99.99% purity) atmosphere with a flow rate of 500 sccm. Subsequently, a flow gas of C_2H_2 (flow rate of 20 sccm) was brought in and mixed with the Ar gas in the tube and the heating process was maintained for 4 h. In the end, the system was cooled to room temperature at Ar gas atmosphere and the Sn-filled CNTs hierarchical architecture membrane on Cu foils was obtained.

2.2. Characterizations. The samples were characterized by field-emission scanning electron microscopy (FE-SEM: HITACHI S-4800) with energy-dispersive X-ray spectroscopy (EDS), transmission electron microscopy (TEM: JEOL JEM-2100), high-resolution transmission electron microscopy (HRTEM: JEOL JEM-2100), X-ray diffraction (XRD: D/max 2550 V), and thermogravimetric analysis (TG: NETZSCH STA409PC).

2.3. Electrochemical Characterizations. The working electrode was prepared by above in situ deposition of Sn-filled CNTs hierarchical architecture on Cu foils. Thin Li foils ($\varphi 16 \times 1.2$ mm) and polypropylene membrane (Celgard 2400) were employed as the counter electrode and separator, respectively. The electrolyte was 1 M $LiPF_6$ dissolved in ethylene carbonate/diethyl carbonate (EC-DEC, 1:1 w/w). The half-cells (CR2016 coin type) were assembled in an argon filled glovebox (Mikrouna Advanced Series) where moisture and oxygen levels were under 0.1 ppm. Cyclic voltammograms and electrochemical impedance spectroscopy of Sn-filled CNTs hierarchical architecture electrode had been characterized by electrochemical workstation (Autolab PGSTAT302N). Galvanostatic charge and discharge experiments of coin cells were tested using on a LAND-CT2001C test system at several different rates (0.1C = 100 mA h g^{-1}, 1C = 1000 mA h g^{-1}) in the voltage range from 0.01 to 2.5 V.

3. RESULTS AND DISCUSSION

The fabrication of the Sn-filled CNTs hierarchical architecture membrane includes two major steps: flame aerosol deposition

(FAD) as illustrated in Figure 1 and chemical vapor deposition (CVD). First, the precursor $SnCl_4$ was sprayed into the flame
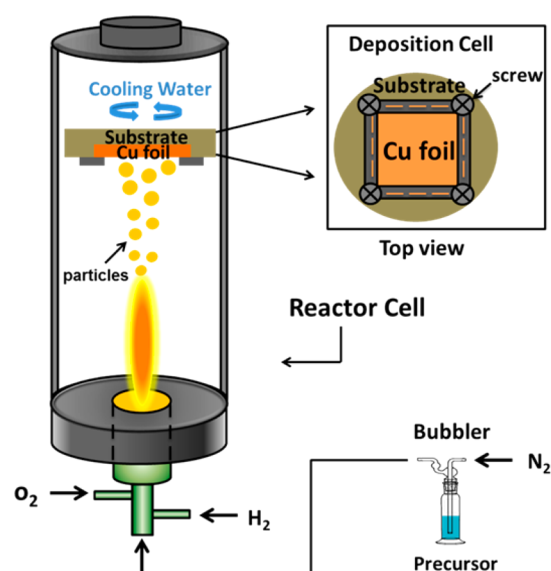
Figure 1. Schematic diagram of flame aerosol deposition (FAD) process.

and hydrolyzed into SnO_2 primary particles with high temperature. After several milliseconds, the primary particles grew larger and agglomerated into SnO_2 nanoparticles. Subsequently, the fresh SnO_2 nanoparticles were directly deposited on the Cu foils fixed on the deposition cell to form a microsize hierarchical SnO_2 membrane, as shown in Figure 2a. Powder X-ray diffraction (XRD) characterization of
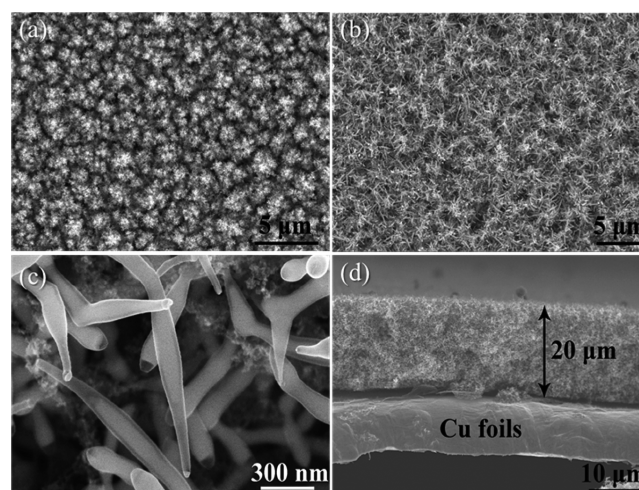

Figure 2. SEM images of (a) SnO_2 membrane; (b, c) Sn-filled CNTs hierarchical architecture; (d) cross-sectional view of Sn-filled CNTs hierarchical architecture membrane.

SnO_2 membrane was carried out (see Figure S1 in the Supporting Information), which presents that all diffraction peaks of black curve are in good agreement with tetragonal rutile SnO_2 (JCPDS No.21−1250). The average diameter of SnO_2 nanoparticles is about 5−10 nm and the hierarchical architectures was assembled by SnO_2 aerosol nanoparticles in in situ flame process. Further, high porosity (Figure 2a) is beneficial to the following formation of carbon shells by CVD.

The prepared SnO$_2$/Cu composite was then transferred into the quartz tube furnace to undergo the CVD process (see Experimental Section for more details). The mechanism of CNTs-growth has been reported previously.[14,28] In brief, when C$_2$H$_2$ went through the 600 °C temperature zone, it decomposed into C and H$_2$, which reduced SnO$_2$ to metal tin. Because of the low melting point (231.9 °C) and catalytic effect of metal tin, the C species dissolved into molten Sn and started to grow carbon nanotubes after saturation. Simultaneously, because of the capillary force, tin was infiltrated into CNTs to form Sn-filled CNTs. Finally, hierarchical architectures of Sn-filled CNTs were obtained. As illustrated in Figure 2b, c, the obtained Sn-filled CNTs hierarchical architectures maintained perfect morphology of the original SnO$_2$ membranes and show similar high porosity. The formation of hierarchical architectures assembled by Sn-filled CNTs is ascribed to the hierarchical SnO$_2$ employed as template. The novel synthetic route preserves the hierarchical architecture and converts the composition of membrane form SnO$_2$ into Sn-filled CNTs, which is expected to improve electrochemical performance of the as-prepared electrode. The corresponding EDS of Sn-filled CNT sample (see Figure S2 in the Supporting Information) demonstrates that the sample is composed of element Sn and C and there is no trace of O element detected, indicating that all SnO$_2$ nanoparticles have been reduced to tin. Figure 2d shows that the Sn-filled CNTs hierarchical architecture is uniformly deposited on Cu foils with a thickness of 20 μm.

The more detailed structure and morphology of prepared Sn-filled CNTs hierarchical architecture was characterized by TEM and HRTEM (Figure 3). After the process of chemical vapor
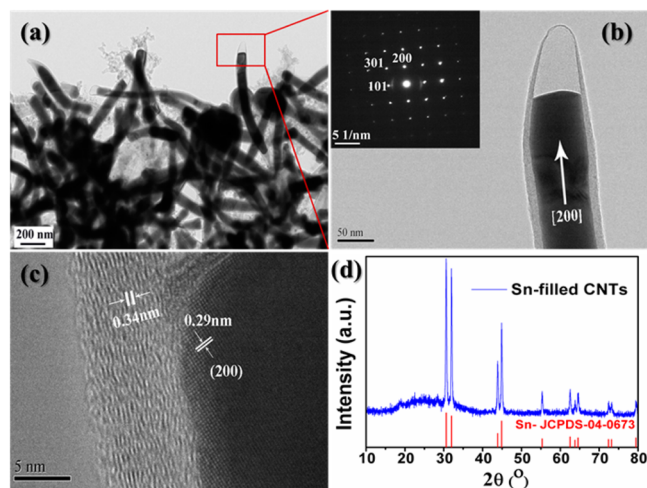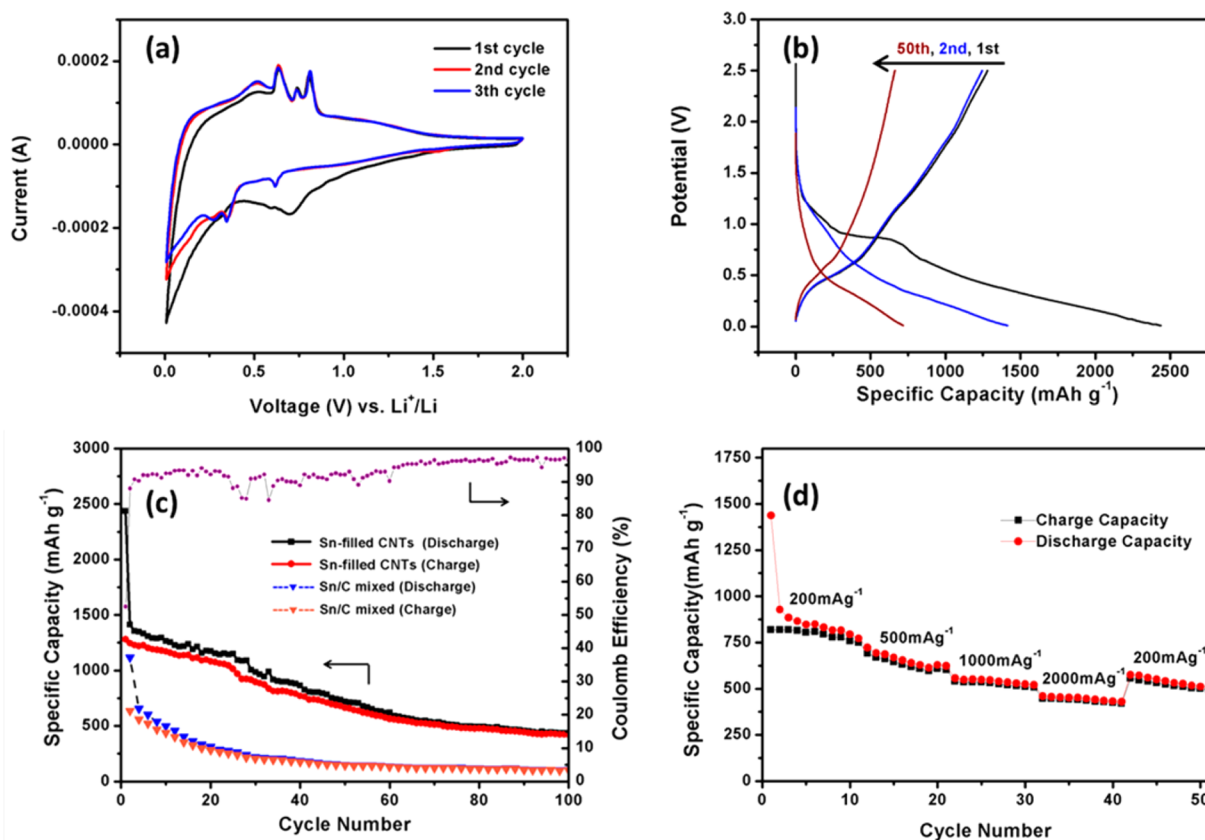

Figure 3. (a)TEM images of Sn-filled CNT hierarchical nanostructure; (b) higher-magnification TEM image confirms metallic tin is confined into CNTs and a vacancy area exists inside of the carbon shell (SAED proves the existence of single-crystalline tin, inset); (c) HRTEM illustrates the thickness of the carbon shell (5−10 nm) and interplanar distance of ~0.29 nm in the (200) crystal plane of Sn; (d) XRD pattern of Sn-filled CNT hierarchical architecture.

deposition, lots of high-aspect-ratio Sn-filled carbon nanotubes toward different directions have been synthesized and staggered into hierarchical nanostructure. The majority of nanotubes have uniform size with a diameter of 40 - 80 nm. The growth direction of the tin filled in the CNTs is along the [200] direction as shown in Figure 3b. More interestingly, an unique

vacancy structure at the top of each nanotube was formed because of not entirely filled in the CNTs of metallic Sn, which is beneficial for accommodating tin volume change during the Li$^+$ intercalation/deintercalation process. Selected area electron diffraction (inset of Figure 3b) demonstrates the existence of single crystalline metallic tin in the interiors of CNTs. Furthermore, XRD pattern of Sn-filled CNTs sample is completely matched with tin (JCPDS No. 04−0673) (Figure 3d), which means SnO$_2$ has been completely reduced to metal tin after the CVD process. The graphitized carbon shell with thickness of 5−10 nm and interplanar distance of 0.29 nm in the (200) crystal plane of Sn could be identified by high resolution TEM image as shown in Figure 3c. The carbon shell plays a critical role in buffering tin volume change and is significant to capacity retaining because of its elasticity and mechanical strength. The Sn-filled CNTs hierarchical structure film was composed of about 81.0 wt % tin and 19.0 wt % carbon calculated by thermogravimetric analysis (TGA) (see Figure S3 in the Supporting Information).

The CV curve of Sn-filled CNTs hierarchical structure electrode was obtained in the voltage range of 0.01−2 V (versus Li/Li$^+$) at a scanning rate of 0.2 mV s^{-1} to investigate the electrochemical processes in regard to Li insertion/extraction (Figure 4a). The three cathodic peaks between 0.25 and 0.62 V during discharging step could be attributed to multistep lithiation of Sn with Li to form Li$_x$Sn ($x < 4.4$) alloy, whereas four distinct peaks at the anode scanning between 0.5 V and 0.8 V can be assigned to delithiation of the Li$_x$Sn alloy.[29−31] The observation that the four oxidation peaks between 0.5 and 0.8 V are quite stable in the first three cycles demonstrates a reversible deintercalation process of lithium ion from the Li$_x$Sn alloy. Meanwhile, we observed a gradual current decrease below 0.25 V with increasing cycles at the cathodic scanning, which might originate from irreversible intercalation of Li$^+$ ions in the carbon shell.[32−34] Moreover, the initial scan on the negative-current side showed a broad reduction peak at 0.7 V, which was quite different from the following scans, indicating a different lithiation route in the initial discharging/alloying process. One explanation of the irreversible peak is the formation of solid electrolyte interphase (SEI) films. Nevertheless, the signal peaks of SEI films on metallic tin are typically at 1.05 and 1.55 V, whereas those on the carbon shell are at 0.8 and 1.25 V.[35] The absence of these signal peaks demonstrated that metallic tin is well-confined inside the carbon shell, whereas the SEI films is formed neither on the carbon nor on the metallic tin. Another possible reason is a series of salt anion reductions caused by decomposed products of LiPF$_6$ and EC/DMC reacting with lithium ions, which usually form SEI films at 0.5−0.8 V (Li/Li$^+$).[36]

Figure 4b shows the voltage profiles of Sn-filled CNTs anode at a current density of 100 mA h g^{-1} between 0.01 and 2.5 V. The first discharge curve displays a steep voltage drop to 1.2 V and a voltage plateau around 0.8 V, which disappears in the following cycles. This observation further certificates that there are a series of electrolyte anion reductions involving lithium ions around 0.5−0.8 V to form SEI films as mentioned above. The initial discharge specific capacity was found to reach relatively high 2437 mA h g^{-1} following with low initial coulomb efficiency of 52.5%. Owing to a different initial lithiation route for the first cycle, the electrode irreversible capacity of 1157 mA h g^{-1} has achieved almost half of initial discharge capacity, which is probably associated with the formation of SEI films, irreversible lithium intercalation into

Figure 4. (a) Cyclic voltammograms of Sn-filled CNTs hierarchical architecture electrode in the voltage range of 2.0−0.01 V (versus Li/Li$^+$) at a 0.2 mV s^{-1} scanning rate; (b) galvanostatic charge/discharge curves of Sn-filled CNT hierarchical architecture anode; (c) cycling performance of Sn-filled CNTs hierarchical architecture and Sn−C mixed anodes at a current density of 100 mA g^{-1}; (d) rate performance of Sn-filled CNT hierarchical architecture electrode at the current density of 200, 500, 1000, 2000, and 200 mA g^{-1}, respectively.

carbon shell and a series of side reactions caused by the decomposition of electrolyte.[35] Apart from the first discharge profile, the following discharge and charge curves almost overlap with each other, indicating a reversible process of lithiation and delithiation. The charge profiles from first to 50th cycle present a plateau around 0.5−0.8 V, which is ascribed to phase transition from Li$_x$Sn to Sn.

The cycling performance of as-prepared Sn-filled CNTs hierarchical architecture anode has been evaluated by galvanostatic charge/discharge cycling at 100 mA g^{-1} current density with cutoff potentials at 0.01 and 2.5 V as shown in Figure 4c. It can be observed that the capacity is above 1000 mA h g^{-1} before first 30 cycles, which is higher than tin theoretical capacity (992 mA h g^{-1}) mainly due to the existence of excessive Li$^+$ storage in SEI films, carbon shells and electrolyte. The coulomb efficiency has increased to above 90% after the first discharge/charge cycle and maintains above 95% after 60 cycles. The CNTs layer with appealing elasticity and tolerance to stress plays a significant role in avoiding the pulverization to some extent, which gives rise to a relatively low rate of capacity fading. The fade rate per cycle before the 50th cycle is calculated to 0.97% and decreases to 0.71% from the 50th to the 100th cycle. The reversible capacity has decreased to 437.5 mA h g^{-1} after 100 cycles. The theoretical designed capacity of Sn-filled CNTs hierarchical architecture electrode (contains 81.0 wt % tin and 19.0 wt % carbon) is calculated to 860.7 mA h g^{-1} (992 × 0.81 + 372 × 0.19 = 860.7). The capacity retained nearly 51% of the designed capacity after 100

cycles, which is quite an improvement in the Sn/C materials anode prepared by our highly efficient synthetic route.

In contrast, we prepared Sn−C mixed powders by physical stirring of commercial tin powders (81 wt %) and carbon black (19 wt %) as anode materials. The initial discharge capacity of Sn−C mixed powders is 1116.4 mA h g^{-1} and sharply drops to 310.7 mA h g^{-1} after 10 cycles. The cycling performance and reversible capacity of Sn-filled CNTs hierarchical architecture anode are obviously superior to the Sn−C mixed powders. The improving cycle life can be mainly ascribed to three merits: (1) the carbon shell with high elasticity and mechanical strength confines metallic tin in the interior space of CNTs and there are many vacancy areas in the CNTs, which can effectively avoid the volume shrinkage/expansion during the alloying/dealloying processes, ensuring high cycle stability.[9] (2) Each Sn-filled CNT toward different directions staggered into 3D hierarchical nanostructure and created amounts of pores, which are beneficial to transmission of Li$^+$ ions. On the other hand, both tin and carbon possess excellent conductivity. These intriguing features not only accelerate the electron transport efficiency during Li$^+$ ions insertion/desertion, but also improve the mechanical properties of the integral matrix, which greatly enhance the reversible capacity and rate performance. (3) The majority of Sn-filled CNTs partly cross-linked with each other, resulting in many junctions. The junctions, combining with 3D hierarchical architecture, can construct a superior conducting network, further enhancing the rate performance.

Furthermore, Figure 4d presents the rate performance of Sn-filled CNTs hierarchical architecture anode under the condition of same discharge and charge current densities. The charge capacity remains above 800 mA g h^{-1} in the current density of 200 mA g^{-1} before the 10th cycle and decreases to 613.7, 524.5, 429.0, and 510.9 mA g h^{-1} in the following each 10 dicharge/charge cycles with the current density of 200, 500, 1000, 2000, 200 mA g^{-1}, respectively. The capacity decreases slowly with higher current density (even as high as 2A g^{-1}), indicating an excellent rate capacity performance, which is attributed to the formation of high efficient Li$^+$ transportation pathways in the 3D conductive network built by the Sn-filled CNTs hierarchical architecture.

Electrochemical impedance spectroscopy (EIS) measurement was carried out to further identify the rate capacity performance of Sn-filled CNTs hierarchical architecture electrode. Figure 5 displays the Nyquist plots (Z' vs $-Z''$,
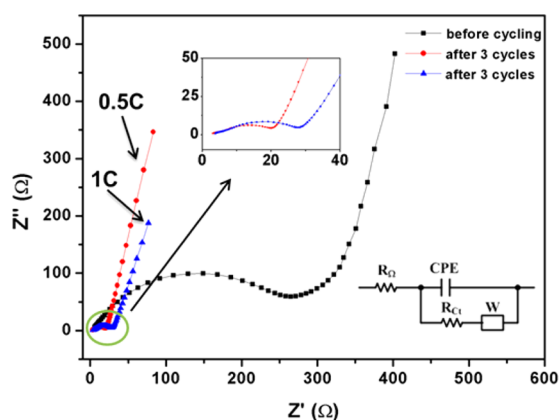
Figure 5. Nyquist plots of Sn-filled CNTs hierarchical architecture electrodes in the frequency range from 0.01 Hz to 100 kHz before and after 3 cycles with 0.5C and 1C cycling rates.

which refer to the real and imaginary parts of the cell impedance, respectively) of Sn-filled CNTs electrodes before and after three discharge/charge cycles with different cycling rates. Each Nyquist plot consists of a depressed semicircle which originates in high frequency (1×10^5 to 200 Hz) and a linear line region in the low frequency belonging to the Warburg region (W). In the equivalent circuit (inset of Figure 5), R_Ω and R_{ct} are the ohmic resistance which refer to integral resistance (composed of the electrolyte, separator, electrical contacts) and charge transfer resistance, respectively.[37] CPE stands for the constant phase-angle element. We observe that the ohmic resistance before cycling ($R_\Omega = 297.2\ \Omega$) is much higher than the ones after three cycles ($R_\Omega = 30.8\ \Omega$ in 0.5C, $R_\Omega = 23.6\ \Omega$ in 1C), which is mainly ascribed to the lack of electrolyte wetting in the electrode materials before cycling. The ohmic resistance of the electrode with higher cycling rate is larger than those with lower cycling rate, which is in agreement with gradually decreasing capacity with increasing current density in the rate capacity performance test. Meanwhile, it is noted that there is no obvious increase in ohmic resistance in high cycling rates, indicating a highly efficient path of Li$^+$ ions in the hierarchical architecture during the rapid charge/discharge process.

4. CONCLUSIONS

In summary, we have fabricated Sn-filled CNTs hierarchical architecture membrane, which is in situ deposited on Cu foils as binder-free electrode by employing both flame vapor deposition and chemical vapor deposition. This novel preparation method of electrode may have potential applications in industry due to the rapid and scalable synthetic route. The Sn-filled CNTs hierarchical architecture electrode shows high cycling life and rate capacity performance in rechargeable LIBs. The Sn-filled CNTs hierarchical architecture anode exhibits 437 mA h g^{-1} after 100 cycles at a current density of 100 mA g^{-1}. Even at as high as 2A g^{-1}, the capacity still maintains above 429 mA h g^{-1}. The improved electrochemical performance is mainly ascribed to great confinement of tin inside of CNTs and superior 3D conducting network constructed by Sn-filled CNTs hierarchical architecture.

■ ASSOCIATED CONTENT

Ⓢ Supporting Information

XRD patterns of as-deposited SnO$_2$ membrane. EDS of Sn-filled CNTs hierarchical architecture membrane. Thermogravimetric analysis (TGA) of Sn-filled CNTs hierarchical architecture. This material is available free of charge via the Internet at http://pubs.acs.org.

■ AUTHOR INFORMATION

Corresponding Author
*E-mail: czli@ecust.edu.cn (C. Z.L.); huyanjie@ecust.edu.cn (Y.J.H.). Fax: +86 21 64250624. Tel: 86-21-6425-0949.

Notes
The authors declare no competing financial interest.

■ ACKNOWLEDGMENTS

■ REFERENCES

(1) Guo, Y. G.; Hu, J. S.; Wan, L. J. *Adv. Mater.* **2008**, *20*, 2878.
(2) Bruce, P. G.; Scrosati, B.; Tarascon, J. M. *Angew. Chem., Int. Ed.* **2008**, *47*, 2930.
(3) Cheng, F. Y.; Liang, J.; Tao, Z. L.; Chen, J. *Adv. Mater.* **2011**, *23*, 1695.
(4) Goodenough, J. B.; Kim, Y. *Chem. Mater.* **2010**, *22*, 587.
(5) Jiang, H.; Lee, P. S.; Li, C. Z. *Energy Environ. Sci.* **2013**, *6*, 41.
(6) Sun, C. W.; Rajasekhara, S.; Goodenough, J. B.; Zhou, F. *J. Am. Chem. Soc.* **2011**, *133*, 2132.
(7) Guo, B. K.; Wang, X. Q.; Fulvio, P. F.; Chi, M. F.; Mahurin, S. M.; Sun, X. G.; Dai, S. *Adv. Mater.* **2011**, *23*, 4661.
(8) Zhang, W. J. *J. Power Sources* **2011**, *196*, 13.
(9) Jiang, H.; Ma, J.; Li, C. Z. *Adv. Mater.* **2012**, *24*, 4197.
(10) Hassoun, J.; Derrien, G.; Panero, S.; Scrosati, B. *Adv. Mater.* **2008**, *20*, 3169.
(11) Yu, Y.; Gu, L.; Wang, C. L.; Dhanabalan, A.; Aken, P. A. V.; Maier, J. *Angew. Chem., Int. Ed.* **2009**, *48*, 6485.
(12) Zou, Y. Q.; Wang, Y. *ACS Nano* **2011**, *5*, 8108.
(13) Luo, B.; Wang, B.; Li, X. L.; Jia, Y. Y.; Liang, M. H.; Zhi, L. J. *Adv. Mater.* **2012**, *24*, 3538.
(14) Luo, B.; Wang, B.; Liang, M. H.; Ning, J.; Li, X. L.; Zhi, L. J. *Adv. Mater.* **2012**, *24*, 1405.

(15) Tricoli, A.; Graf, M.; Mayer, F.; Kühne, S.; Hierlemann, A.; Pratsinis, S. E. *Adv. Mater.* **2008**, *20*, 3005.

(16) Thimsen, E. *Chem. Mater.* **2011**, *23*, 4612.

(17) Liu, Y.; Koep, E.; Liu, M. L. *Chem. Mater.* **2005**, *17*, 3997.

(18) Paul, R. P. *Combust. Inst.* **2007**, *31*, 1773.

(19) Rosner, D. E. *Ind. Eng. Chem. Res.* **2005**, *44*, 6045.

(20) Liu, J.; Hu, Y. J.; Li, C. Z. *J. Phys. Chem. C* **2010**, *114*, 5867.

(21) Rao, P. M.; Zheng, X. L. *Nano Lett.* **2011**, *11*, 2390.

(22) Byeon, J. H.; Kim, J. W. *ACS Appl. Mater. Interfaces* **2010**, *2*, 947.

(23) Kim, L.; Nam, T.-H.; Kim, K.-W.; A., J.-H.; Park, D.-S.; Ahn, C.; Chun, B. S.; Wang, G.; Ahn, H.-J. *Nanoscale Res. Lett.* **2012**, *7*, 64.

(24) Rao, P. M.; Zheng, X. L. *Nano Lett.* **2009**, *9*, 3001.

(25) Chew, S. Y.; Patey, T. J.; Waser, O.; Ng, S. H.; Büchel, R.; Tricoli, A.; Krumeich, F.; Wang, J.; Liu, H. K.; Pratsinis, S. E.; Novák, P. *J. Power Sources* **2009**, *189*, 449.

(26) Liu, Y.; Liu, M. L. *J. Am. Ceram. Soc.* **2004**, *87*, 2139.

(27) Liu, Y.; Dong, J.; Hesketh, P. J.; Liu, M. L. *J. Mater. Chem.* **2005**, *15*, 2316.

(28) Hsu, K.-C.; Liu, C.-E.; Chen, P.-C.; Lee, C.-Y.; Chiu, H.-T. *J. Mater. Chem.* **2012**, *22*, 21533.

(29) Deng, D.; Lee, J. Y. *Angew. Chem., Int. Ed.* **2009**, *48*, 1660.

(30) Zhang, W.-M.; Hu, J.-S.; Guo, Y.-G.; Zheng, S.-F.; Zhong, L.-S.; Song, W.-G.; Wan, L.-J. *Adv. Mater.* **2008**, *20*, 1160.

(31) Marcinek, M.; Hardwick, L. J.; Richardson, T. J.; Song, X.; Kostecki, R. *J. Power Sources* **2007**, *173*, 965.

(32) Aurbach, D.; Markovsky, B.; Weissman, I.; Levi, E.; Ein-Eli, Y. *Electrochim. Acta* **1999**, *45*, 67.

(33) Wu, G. T.; Wang, C. S.; Zhang, X. B.; Yang, H. S.; Qi, Z. F.; He, P. M.; Li, W. Z. *J. Electrochem. Soc.* **1999**, *146*, 1696.

(34) Ahn, D.; Xiao, X.; Li, Y.; Sachdev, A. K.; Park, H. W.; Yu, A.; Chen, Z. *J. Power Sources* **2012**, *212*, 66.

(35) Jung, Y. S.; Lee, K. T.; Ryu, J. H.; Im, D.; Oh, S. M. *J. Electrochem. Soc.* **2005**, *152*, A1452.

(36) Aurbach, D.; Zaban, A.; Ein-Eli, Y.; Weissman, I.; Chusid, O.; Markovsky, B.; Levi, M.; Levi, E.; Schechter, A.; Granot, E. *J. Power Sources* **1997**, *68*, 91.

(37) Zhang, C. F.; Peng, X.; Guo, Z. P.; Cai, C. B.; Chen, Z. X.; Wexler, D.; Li, S.; Liu, H. *Carbon* **2012**, *50*, 1897.